

# **Optimizing Tritium Recovery with Commercial Heat Exchangers to Advance Commercial Fusion Energy**

## **Final Report**

### **Team 42**

Sean Shitamoto  
Esteban Labrador  
Sascha Turovskiy

### Advised by:

Guanyu Su  
Ben Li

## Table of Contents:

Executive Summary	4
Section 1: Introduction and Preliminary Design Choices	4
What is the Problem with Tritium?	4
Existing Methods of Extraction	5
Heat Exchanger Design Choice	5
Section 2: How the Project Studied the Potential of Commercial CHXs to be Used for Tritium Extraction	7
Software Used to Simulate Studies	7
Setting up the Simulations	8
Control Geometry and Explored Parameters	10
Mesh Sensitivity Analysis	11
Formulation of the Mass Transfer Coefficient	14
Channel Size Study	14
Channel Orientation Study	16
Zigzag bend angle study	19
Segment length study	24
Main Takeaways and Recommendations for Future Designs to Optimize Tritium Extraction	27
References	29
Appendix	31
Appendix A.1: Physical Constants and Properties of FLiBe and 316SS	31
Appendix A.2: Simulation Continua Physical Models Chosen	33
Appendix A.3: Inlet Tritium Concentration Calculation	35
Appendix A.4: Simulation Mesh Settings Chosen	36

## List of Figures:

Figure 1: (a) Microchannels (red) etched into a metallic plate. (b) A cut-section view of multiple plates stacked on top of each other with one layer of FLiBe (red) and vacuum (blue) highlighted. (c) A single zigzag channel of FLiBe (red) and vacuum (blue) cut out of the grid.	6
Figure 2: Heat exchanger geometry and zooming in on an example unit channel geometry being simulated.	7
Figure 3: Example mesh of the FLiBe geometry showing a small, relatively consistent cell size.	8
Figure 4: Geometric values and BCs which include periodic BCs (in green and purple), partial pressure and flux continuity BC at the FLiBe-316SS interface, and a zero tritium concentration BC at the vacuum-316SS interface.	9
Figure 5: Relative tritium concentration as tritium travels from FLiBe through a metal and into a vacuum. Tritium dissociation and recombination is depicted at the FLiBe-metal and metal-vacuum interfaces respectively.	10
Figure 6: (a) Zigzag channel with 1 hot channel (red) and a vacuum channel on bottom (blue). (b) Geometric dimensions of the default zigzag channel[13].	11
Figure 7: Laminar (top) and Turbulent (bottom) mesh study results comparing total FLiBe region cell count vs surface integrated flux.	13
Figure 8: Cross sections of turbulent regime FLiBe mesh. 0.5mm (top left), 0.25mm (top right), 0.1mm (bottom left), and 0.05mm (bottom right).	14

Figure 9: Channel size differences, Small (left) and Large (right).	15
Figure 10: MTC over channel length for Small and Large channel sizes under laminar and turbulent regimes.	16
Figure 11: Channel orientation differences: 1-1 Vertical (top left), 1-1 Horizontal (top right), Burger (bottom left), and 2-1 (bottom right). Red indicates FLiBe channel and white indicates vacuum.	17
Figure 12: MTC over channel length for each orientation under laminar (top) and turbulent (bottom) regimes.	18
Figure 13: Mass transfer coefficient (MTC) as a function of distance along the channels for varying channel bend angles and flow rates.	21
Figure 14: Top-down cut-section view of the turbulent velocity profiles in 180 (top-left), 140 (top-right), 100 (bottom-left) and 60 (bottom-right) channels	21
Figure 15: Plot of average MTC with respect to Reynolds number. Four points are plotted for laminar and turbulent flow regimes with the plots showing increasing Reynolds numbers for decreasing bend angle.	23
Figure 16: Plot of average MTC with respect to flow-normalized pressure drop. Four points are plotted for laminar and turbulent flow regimes with the plots showing increasing pressure drop for decreasing bend angle.	24
Figure 17: Top View of Velocity Field and Its Influence on Mass Transfer Coefficient Along the Z-Axis	25
Figure 18: Mass transfer coefficient (MTC) as a function of distance along the channels for varying channel length segments and flow rates.	26

## List of Tables:

Table 1: Existing methods of tritium extraction.	5
Table 2: Average MTC for each channel size under both regimes.	15
Table 3: Flow rate-normalized pressure drops for each channel size under both regimes.	16
Table 4: Average MTC for each orientation under both regimes.	19
Table 5: Flow rate-normalized pressure drops for each orientation under both regimes.	19
Table 6: The 4 bend angle geometries being studied	20
Table 7: Average MTC for each orientation under both regimes.	22
Table 8: Flow rate-normalized pressure drops for each orientation under both regimes.	22
Table 9: Average MTC for each orientation under both regimes.	26
Table 10: Flow rate-normalized pressure drops for each orientation under both regimes.	27
Table 11: Table of STAR-CCM+ Field Functions and Tables	32
Table 12: Continua Physics Model settings for FLiBe and 316SS regions under laminar and turbulent regimes.	34
Table 13: Bulk Mesh and Prism Layer settings for FLiBe and 316SS regions under laminar and turbulent regimes.	38

## Executive Summary

Tritium is a fuel source for nuclear fusion power plants. Manufacturing tritium is exorbitantly expensive, and so modern fusion energy devices like Commonwealth Fusion System's Affordable, Robust, and Compact fusion device are designed to utilize molten salt to produce it. One difficulty with this method of producing tritium is figuring out how to reclaim the tritium from the salt to be used in subsequent fuel cycles. This project aims to investigate potential geometries of Permeation Against Vacuum (PAV) heat exchangers that would drive tritium diffusion out of such molten salt, in particular FLiBe salt. PAV heat exchangers in particular are investigated because of the inherent concentration gradients that drive diffusion due to the presence of a vacuum. The team utilized StarCCM+ computational fluid dynamics (CFD) software for physics modeling and analysis with the aim of discovering trends in designs that may or may not induce such tritium diffusion from the FLiBe salt. Performance of tritium transfer from the salt in a specific PAV design is quantified with the mass transfer constant, and the team discovered that there were minimal differences in tritium transfer when changing the channel diameters or orientations. But when changing the channel bend angle, a sharper angle aided in tritium extraction. Additionally, a slightly shorter segment length aided in tritium extraction. The results are promising and for future studies, the team recommends simulating or investigating different materials, types of heat exchangers, and performing a physical validation experiment. Since this project was fully focused on analysis using CFD, it would be worthwhile to conduct a physical experiment with a specific selected geometry such as the base case of 100 degrees and 4.75mm segment lengths to get a realistic assessment of its ability to transport tritium and to assess the validity of the project's simulations.

## Section 1: Introduction and Preliminary Design Choices

### What is the Problem with Tritium?

Fusion energy has the potential to satisfy humanity's hunger for energy at extremely low pollution to the environment, helping to prevent climate change [12]. Fusion energy production is an ongoing process with many details yet to be solved. Regardless of method, one of the key bottlenecks for the commercialization of these systems is how the fuel is sourced. The primary energy-releasing reaction used is the deuterium-tritium (DT) fusion reaction. It is incredibly energy dense, producing a million times more energy per unit mass than coal.

Deuterium is easy to source as it is naturally abundant in seawater, but problems arise with sourcing tritium. Since tritium is too scarce to collect from any natural source, the main way tritium is sourced is by manufacturing. Tritium production is an expensive process as only a few nuclear reactors are specifically used to produce it, but scientists have come up with other ways to produce it within a fusion device.

Molten salts, like FLiBe and LiPb, are utilized within a fusion device's breeding blanket which surrounds where the DT reaction occurs [1]. These molten salts in the breeding blankets are the tritium breeders, as tritium atoms are produced through reactions with lithium when exposed to neutron irradiation. Some examples of such designs include Commonwealth Fusion System's Affordable, Robust, Compact (ARC) and Xcimer Energy's fusion devices which both utilize FLiBe. A different molten salt, LiPb, is being studied within theoretical models like the DEMO

DCLL and DEMO WCLL [1][2]. The main problem comes from extracting the bred tritium to be used in future fuel cycles with various strategies being studied.

#### Existing Methods of Extraction

There are a number of methods already utilized to remove tritium from FLiBe, including electrolysis and oxidation, gas-liquid contactors (LGCs), liquid-vacuum contactors (LVCs), spray devices, and permeator against vacuum (PAV) devices. A brief description of these techniques can be found below in Table 1:

Method	Description
Electrolysis and Oxidation	An electric current is used to break down FLiBe into its chemical components before separating them [5]
LGC and LVC	A sweep gas such as argon or helium is used to blow over or through FLiBe to mix and collect tritium in its gaseous state. Once collected, the tritium is swept away and collected [6].
Spray	A fine mist of salt is dispersed into a sweep-gas to separate away the tritium and collect it [4].
PAV	A large surface area of hydrogen-permeable metal is used as a filter to passively separate the tritium from FLiBe [6].

Table 1: Existing methods of tritium extraction.

PAV devices offer several advantages due to their passive functionality, high efficiency, and applicability to existing heat exchanger designs. Of key importance to the project is their high extraction efficiency and simplicity of operation by leveraging a concentration difference between the FLiBe and vacuum.

Determining a design that is most efficient at tritium removal while being cost-effective for the commercialization of fusion energy production has been a challenge. Many existing PAV designs are custom designs that may efficiently remove tritium but are not cost-effective. Because tritium removal is benefited by increased surface area, some research has gone into verifying whether commercial heat exchanger designs can be used as PAV designs. Such designs include plate and frame, double tube in tube, pillow plates, and printed circuit heat exchangers.

#### Heat Exchanger Design Choice

Our project aimed to improve tritium extraction using commercial heat exchangers by implementing a PAV system based on a Printed Circuit Heat Exchanger (PCHE) design with

microchannels. Figure 1 shows how these PCHEs are fabricated by etching microchannels into sheets of 316 stainless steel (316SS) and stacking them on top of each other to create a grid. In some channels, FLiBe flows as the tritium carrier. By applying a vacuum on the other channels, concentration gradients are established, allowing tritium to diffuse from FLiBe through a metal and into the vacuum. The PCHE's compact design minimizes material usage (in tandem with 316SS's relatively low cost) while providing a large transport area for tritium extraction, making it cost-effective.

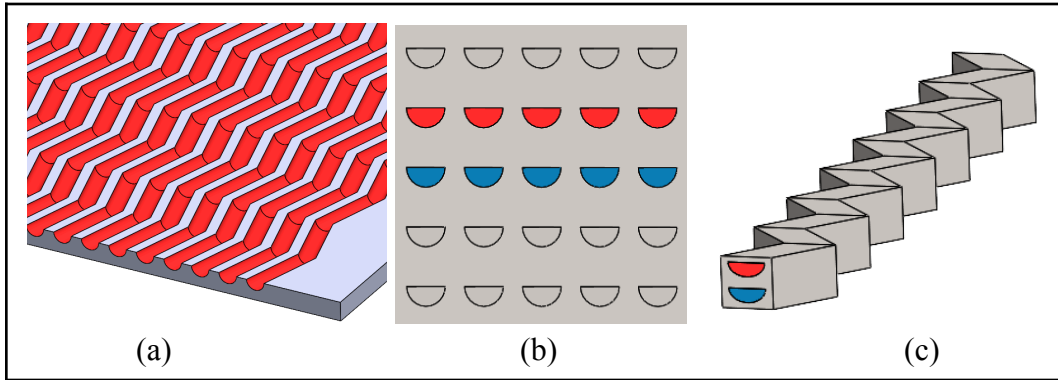


Figure 1: (a) Microchannels (red) etched into a metallic plate. (b) A cut-section view of multiple plates stacked on top of each other with one layer of FLiBe (red) and vacuum (blue) highlighted. (c) A single zigzag channel of FLiBe (red) and vacuum (blue) cut out of the grid.

A key feature of the studied PCHE is the zigzag path followed by the microchannels. This design choice aims to enhance tritium transfer in 2 main ways. First, the zigzag microchannels provide a larger transfer surface area per unit volume compared to straight channels, which is crucial for efficient tritium extraction. Second, the zigzag path can introduce turbulence in the fluid flow, which helps further increase convective heat and mass transfer. This turbulence enhances the mass transfer of tritium from FLiBe through the 316SS structure, further improving the efficiency of the extraction process.

While the zigzag channels offer superior tritium extraction performance, they also result in higher pressure drops compared to straight channels. This trade-off must be considered in the design to ensure optimal performance under the given operating conditions. However, the benefits of the zigzag design, combined with the compactness of the PCHE, make it an ideal choice for applications where size is a constraint. The compact design contributes to cost-effectiveness and improved overall system efficiency, making it a promising solution for enhancing tritium extraction. By leveraging these advantages, the zigzag microchannel design in a PCHE can significantly enhance tritium extraction efficiency while maintaining a compact and cost-effective system.

This project was fully simulation based, simulating various PCHE designs in Siemens' StarCCM+ CFD software for heat and mass transport analysis. A design's mass transfer coefficient was calculated and analyzed as a key performance metric, as well as flow rate-normalized pressure drops. Much of the key physical relationships describing tritium mass transport within these systems are derived from work done by K. Dolan, G. Su, and G. Zheng [3]. While some relationships emerged, such as turbulent regimes having pressure drop costs that

outweigh the increased mass transfer compared to laminar regimes, the team would suggest some further investigation to select a single geometry to push towards feasible and useful experimentation.

## Section 2: How the Project Studied the Potential of Commercial CHXs to be Used for Tritium Extraction

### Software Used to Simulate Studies

To study tritium mass transport in PCHEs, the team used Computational Fluid Dynamics (CFD) Software Siemens StarCCM+ (STAR). This software enables users to create a model and simulate it by configuring various parameters within a feature tree. The feature tree includes items such as geometry, continua, regions, interfaces, etc.. Model setup begins with the definition of the geometry.

In the geometry tree branch, one can make a 3D geometry in STAR or import one from a Computer Aided Design (CAD) software. Solidworks CAD was used to create the 3D model before importing it into STAR for meshing. As shown by Figure 2, only a channel unit (a repeated set of FLiBe and vacuum channels) was modeled to keep computational time down. This becomes especially important when creating the mesh of the geometry.

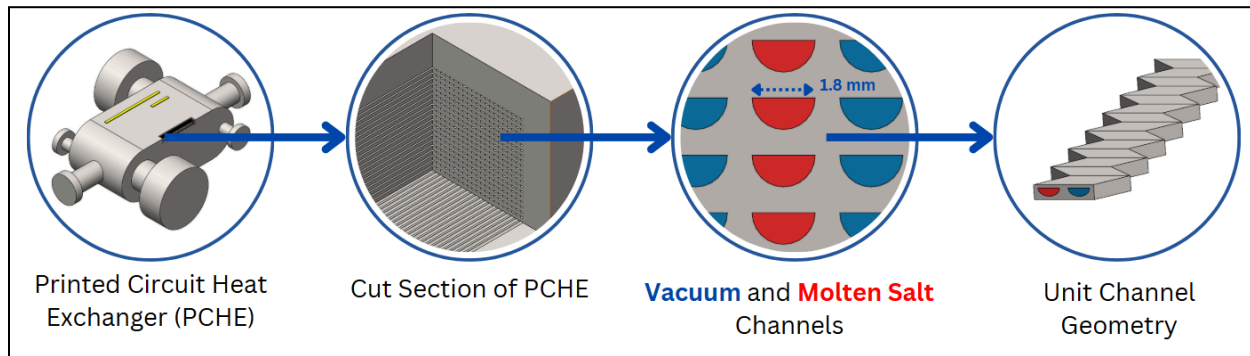


Figure 2: Heat exchanger geometry and zooming in on an example unit channel geometry being simulated.

Meshing cuts the entire geometry into small cells as seen in Figure 3 below. The small cells are used to solve the complicated partial derivative equations of mass and energy transport. Solving this problem is similar to integration where one cuts up a plot into small portions where the smaller the portion size is, the more accurate the integration. Thus, the smaller the mesh cells, the more accurate the solution. But the more cells there are, the longer a simulation takes. So choosing the mesh size is a balance between accuracy and computation time and power. To determine this balance, a mesh study was performed as detailed later in the Mesh Sensitivity Analysis section. Once the geometry is meshed, the relevant continua are added to the simulation.

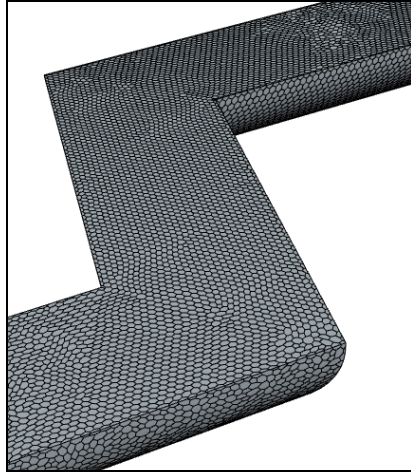


Figure 3: Example mesh of the FLiBe geometry showing a small, relatively consistent cell size.

### Setting up the Simulations

Every aspect of the simulation must be defined, including the constants, properties, and physical equations of the materials being simulated. In particular, these must be defined for the FLiBe and 316SS. The properties for FLiBe and some physics involving the 316SS are not defined by default in STAR-CCM+. A summary of the constants, properties, and equations implemented can be found in Appendix A.1. Generally, they specify diffusion coefficients, concentration of tritium, densities, diffusion functions in FLiBe, and more.

The continua models added to the simulation define what physics is being simulated, and a list of these models can be found in Appendix A.2. Depending on which case was running, the simulations utilized either laminar or turbulent continua models. Both 316SS and FLiBe were treated as liquids, allowing for the creation of a passive scalar for each continuum and enabling the simulation of tritium transport. After selecting the relevant continua models, initial conditions (ICs) and boundary conditions (BCs) were set.

ICs set the simulation's starting point for certain parameters. ICs for both the 316SS and FLiBe included the temperature at 900K, which would occur in a transient system since heat transfer out of the system is nonexistent. Additionally, both are set to start with a zero passive scalar concentration. The 316SS is set to be stationary, how it retains its "solid" nature in STAR. Once the ICs are set and the simulation begins, BCs are used to keep the simulation running properly.

BCs are used in CFD to provide the software points of reference to solve the fluid flow partial differential equations and relevant mass transfer equations. An example includes the inlet and outlet BCs which specify the velocity of FLiBe entering the PCHE channel, what concentration of passive scalar the FLiBe enters with, and how the simulated FLiBe behaves at the end of the simulated channel. For the inlet FLiBe velocities, they were 1 or 15 m/s for the laminar and turbulent cases respectively, while the inlet carried a passive scalar concentration of  $1.52\text{e-}4 \text{ mol/m}^3$  (from ARC tritium breeding rates, derivations of which found in Appendix A.3).



Other BCs included those shown in Figure 4 below. Two conditions were periodic boundaries, which take two separate surfaces and mirror each other to behave as if they were in contact. Periodic BCs are used between the top and bottom as well as the left and right surfaces of the 316SS to simulate the channel as part of a grid of channels. Implementing the periodic BCs is one way computational time was significantly reduced. Two other important BCs included the two fluid-solid interfaces.

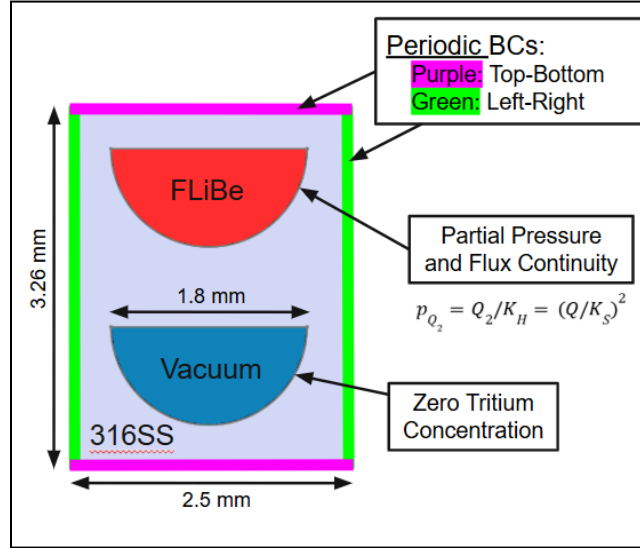


Figure 4: Geometric values and BCs which include periodic BCs (in green and purple), partial pressure and flux continuity BC at the FLiBe-316SS interface, and a zero tritium concentration BC at the vacuum-316SS interface.

The first fluid-solid interface was between the FLiBe and 316SS. The FLiBe-316SS interface is a critical aspect of the simulation and the behavior of tritium across it is shown in Figure 5. In the passive scalar model, tritium exists as  $T_2$  in FLiBe. The  $T_2$  then dissociates into atomic tritium  $2T$  upon reaching the FLiBe-316SS interface and entering 316SS. To incorporate this physical process into the simulation, a BC is applied to multiply by 2 the passive scalar value that enters the 316SS. Since FLiBe is a liquid, it follows Henry's law, while the solid 316SS adheres to Sievert's law. These differences all contribute towards a concentration jump at the interface.

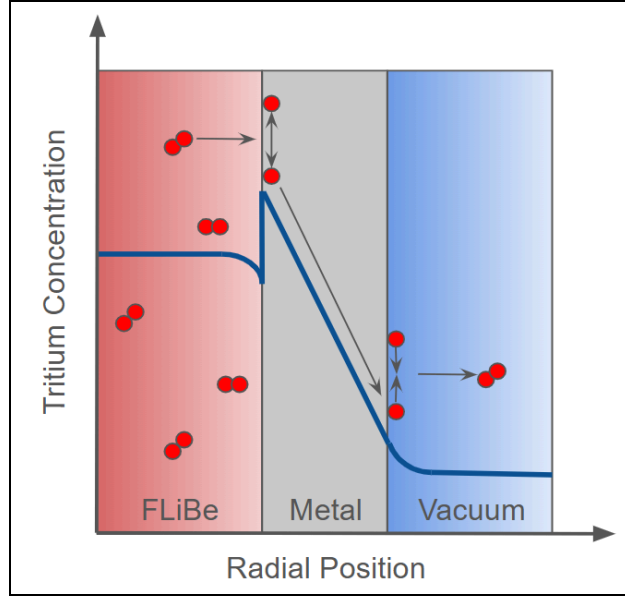


Figure 5: Relative tritium concentration as tritium travels from FLiBe through a metal and into a vacuum. Tritium dissociation and recombination is depicted at the FLiBe-metal and metal-vacuum interfaces respectively.

Using the notation of  $Q_2$  to represent a diatomic molecule of hydrogen isotopes, the partial pressure continuity BC for the FLiBe-316SS interface relating concentration of  $Q_2$  in FLiBe and  $Q$  in the 316SS is as follows in Equation E.1.

$$p_{Q_2} = Q_2/K_H = (Q/K_S)^2 \quad (E.1)$$

$p$ : partial pressure  
 $K_H$ : Henry's law solubility coefficient  
 $K_S$ : Sievert's law solubility coefficient

The second fluid-solid interface is at the 316SS-vacuum boundary. The vacuum is not being meshed to save on computing power and time that would have been required to simulate it. It can be comfortably removed as the vacuum's behavior on the system can be modeled simply as a zero passive scalar concentration right at the border. This zero passive scalar concentration assumes that any passive scalar that reaches the border is immediately swept away.

#### Control Geometry and Explored Parameters

The geometry chosen as the control for simulation was a zigzag geometry with one FLiBe and one vacuum channel as seen in Figure 6. The channels are oriented vertically above and below each other with the zigzag bending at angles of 100 degrees, and the segment lengths between each bend are 4.75mm long. From here, four different studies were conducted: channel size, channel orientation, zigzag bend angle, and segment length. Before running the studies, the mesh needed to be analyzed to ensure accurate results.

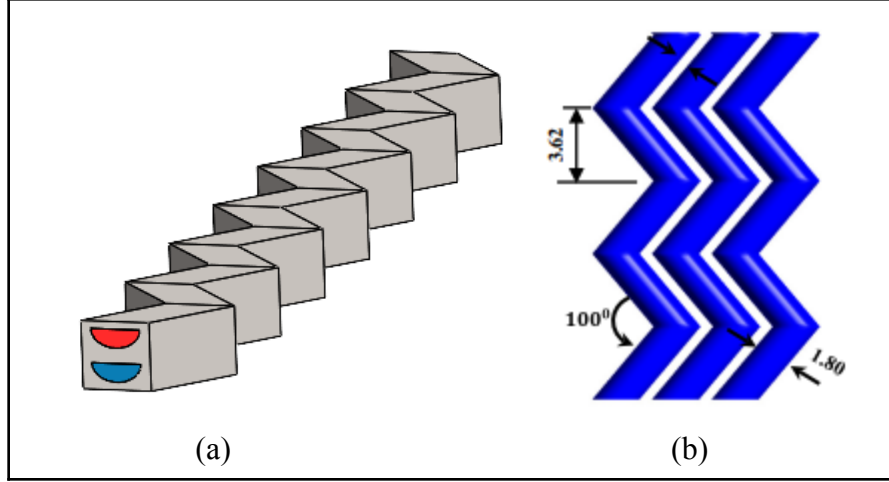


Figure 6: (a) Zigzag channel with 1 hot channel (red) and a vacuum channel on bottom (blue). (b) Geometric dimensions of the default zigzag channel[13].

### Mesh Sensitivity Analysis

The mesh sensitivity analysis is performed to ensure that the mesh is sufficiently refined so that the simulation results are not heavily affected by further refinement of the mesh. This analysis requires running a simulation of the control geometry multiple times with varying levels of mesh refinement. A figure of merit is taken from each simulation to compare with each other as a function of cell numbers. The mesh is continually refined with the number of cells increasing until the plot plateaus. Once the plot plateaus, it is indicative of the mesh being sufficiently refined and the simulations can move on to the channel size, channel orientation, zigzag bend angle, and segment length studies with the associated mesh settings.

Two mesh sensitivity analyses, one each for the laminar and turbulent regimes, were run. While a detailed list of mesh settings chosen can be found in Appendix A.4, the main difference in the meshes between the two regimes can be seen in the prism layers (the meshing along the boundary of a region) in the FLiBe region. For the laminar regime, there were 5 prism layers and their thickness was scaled as a percentage of the base mesh size, while for the turbulent regime there were 3 prism layers and were set to have a total absolute thickness of 0.15mm. The rationale for the turbulent regime prism layer setting was to account for the  $y^+$  region of the turbulent boundary flow and was calculated to be 0.75mm using the Equations E.2 through E.4 below, while this was not a concern for the laminar regime [14]. The thickness was reduced from 0.75mm to 0.15mm because the calculated thickness was much too large for the channel size (with a radius of 0.9mm) and because it was found that a consistent thickness is a more significant factor than the total thickness.

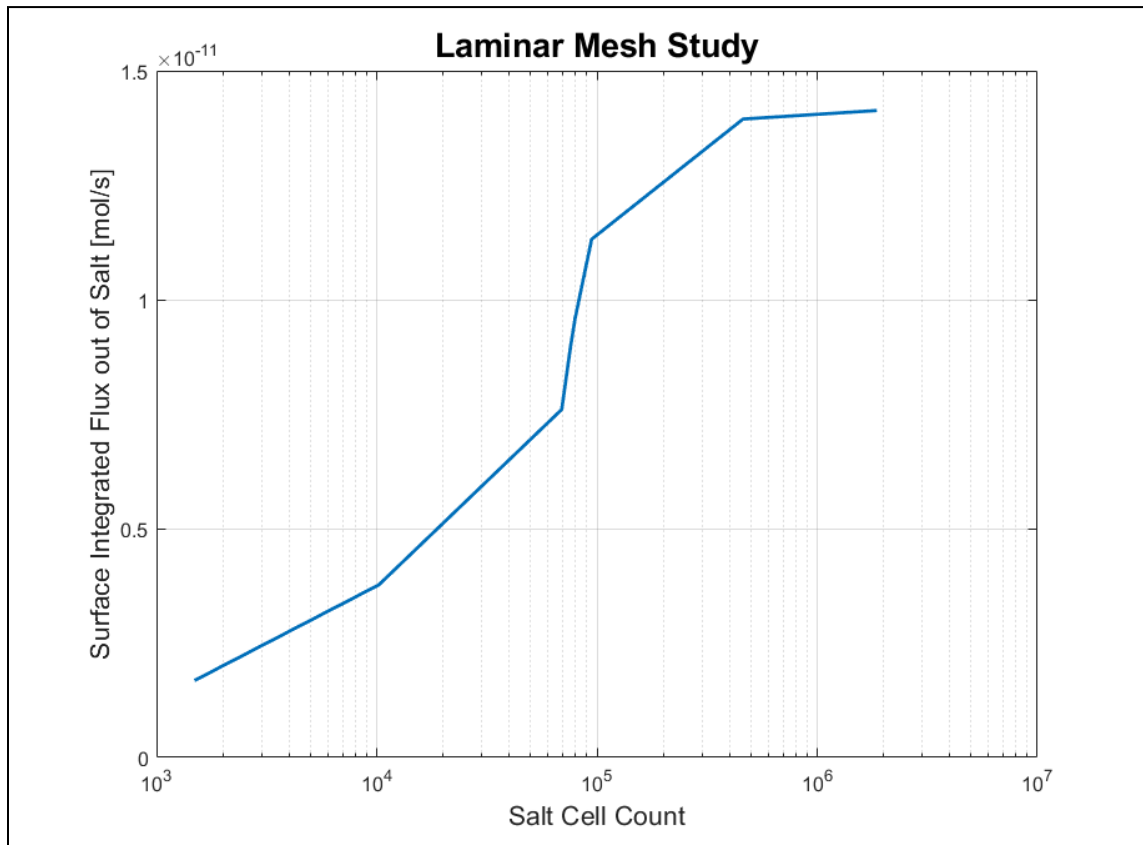
$$y^+ = \frac{yu_\tau}{\nu} \quad (\text{E.2})$$

$$u_\tau = \sqrt{\frac{\tau_w}{\rho}} \quad (\text{E.3})$$

$$\tau_w = \rho \nu \left( \frac{d\langle U \rangle}{dy} \right)_{y=0} \quad (\text{E.4})$$

$y$ : absolute distance from the wall  
 $\nu$ : kinematic velocity  
 $u_\tau$ : friction velocity  
 $\tau_w$ : wall shear stress  
 $\rho$ : density  
 $\langle U \rangle$ : mean bulk velocity

Within each regime, the base mesh size of the FLiBe regions were refined. These values were 5mm, 2.5mm, 1mm, 0.75mm, 0.5mm, 0.25mm, 0.1mm, and 0.05mm. The base mesh size of the 316SS was kept to 0.5mm as flow patterns would not change with refinement. As the base mesh size goes down, the total cell counts rise multiple magnitudes. The relationship between the rise in cell count and a figure of merit was graphed and analyzed to determine the optimal mesh, both for accuracy and simulation runtime. The figure of merit chosen was the surface integrated flux from the FLiBe into the 316SS. As the geometry is kept constant, the total surface area of the FLiBe region remains constant as well, and thus the surface integrated flux was expected to converge. All simulations were run until as many residuals as possible fell below  $1e-4$  or until they plateaued, and below in Figure 7 the results of the mesh study can be seen:



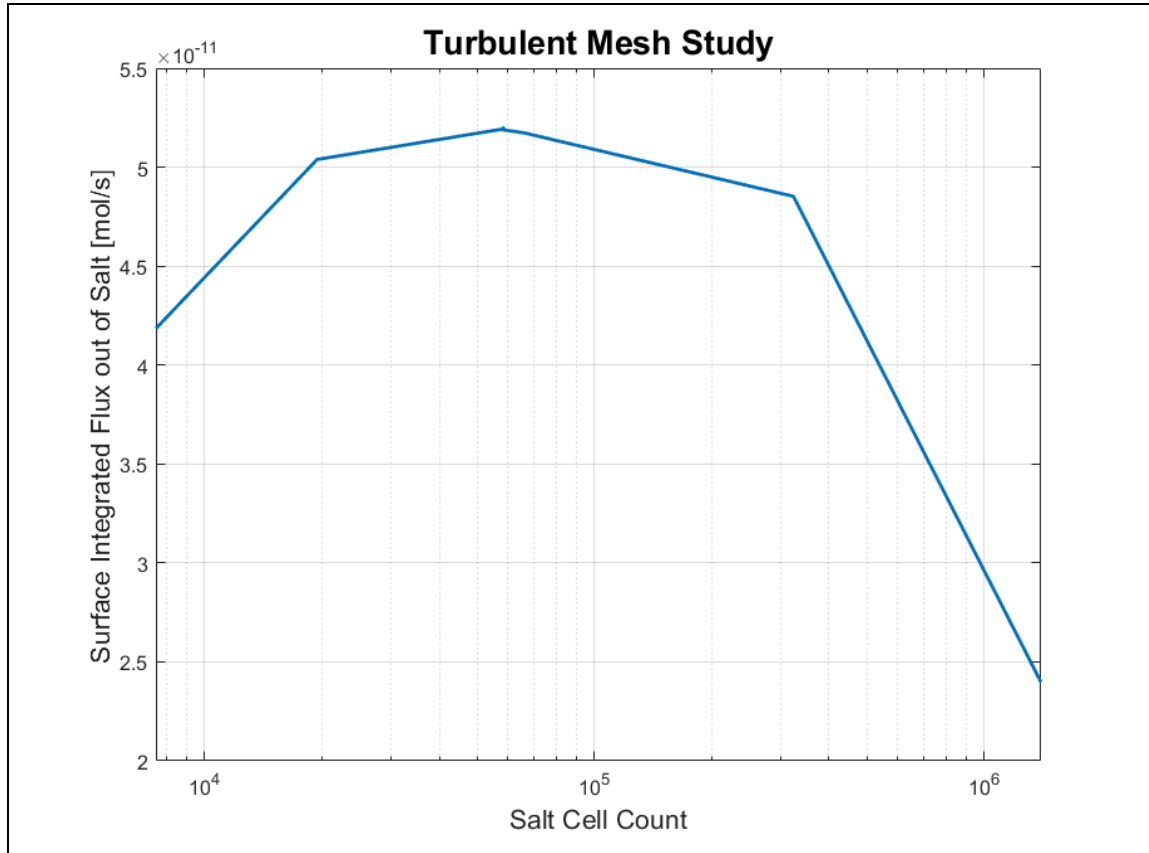


Figure 7: Laminar (top) and Turbulent (bottom) mesh study results comparing total FLiBe region cell count vs surface integrated flux.

From Figure 7, a convergence of the surface integrated flux in the laminar regime is shown towards the finest two meshes tested (0.1mm and 0.05mm base mesh sizes). The difference constituted a 1.34% change between the last two flux values. As the finest mesh takes significantly longer to run due to the increase in cell counts, the FLiBe region base mesh size of 0.1mm for the laminar regime was chosen.

The decision for the turbulent regime's mesh is more difficult, as the finest mesh shows a significant drop in flux when compared to the rest of the meshes. On closer inspection, the mesh's prism layers' did not have the same thickness for the finest mesh, as shown below in Figure 8. As the prism layer thickness decreases significantly for the 0.05mm mesh and the change in flux between the 0.25mm and 0.1mm was only 6.21%, the 0.25mm mesh was chosen for the turbulent regime.

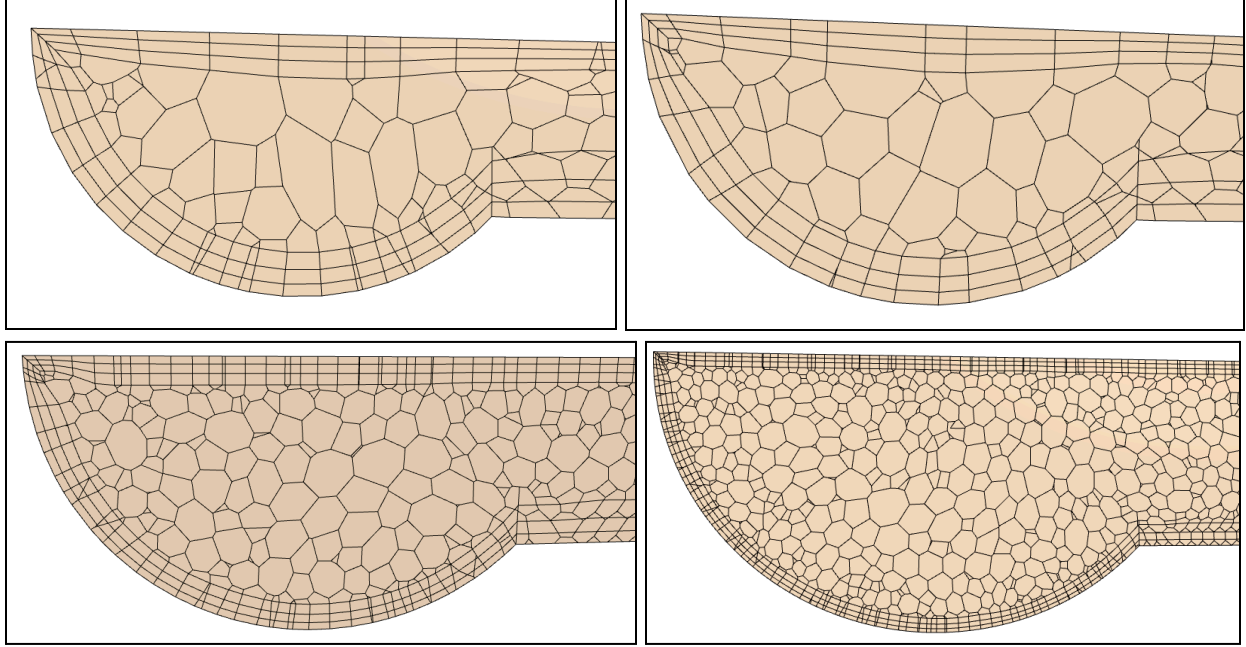


Figure 8: Cross sections of turbulent regime FLiBe mesh. 0.5mm (top left), 0.25mm (top right), 0.1mm (bottom left), and 0.05mm (bottom right).

#### Formulation of the Mass Transfer Coefficient

To fairly compare all geometries with one another, another figure of merit, the mass transfer coefficient (MTC) is used. The MTC, as seen in Equation E.5 below, normalizes the passive scalar flux by the concentration difference between the FLiBe and vacuum regions. The resulting units of the MTC are in [m/s], which means the MTC characterises the average rate by which the passive scalar is transported from the FLiBe to the vacuum.

$$MTC = \frac{q_{FLiBe \text{ to Metal}}}{C_{FLiBe} - C_{Vacuum}} \quad (E.5)$$

From Equation E.5, there are three main components. First, in steady state the flux of passive scalar from the FLiBe to the 316SS becomes equivalent to the flux from the 316SS to the vacuum. This relationship has been observed in simulations and makes sense as it indicates that in steady state there is an equal amount of mass entering and exiting the 316SS, and allows for using the flux from the FLiBe to 316SS to characterize the mass transfer from FLiBe to the vacuum region. Second, the first concentration term is taken as the average concentration within the bulk FLiBe region. Lastly, the concentration in the vacuum was taken to be zero.

#### Channel Size Study

In the channel size study, the control geometry was compared to another geometry with all parameters kept the same except for the cross-sectional area of the FLiBe and vacuum channels. For this study's labeling, the geometries were named "Small" and "Large" respectively. Below in Figure 9 shows the differences in the channel sizes, with the Large channels being 30.54% larger.

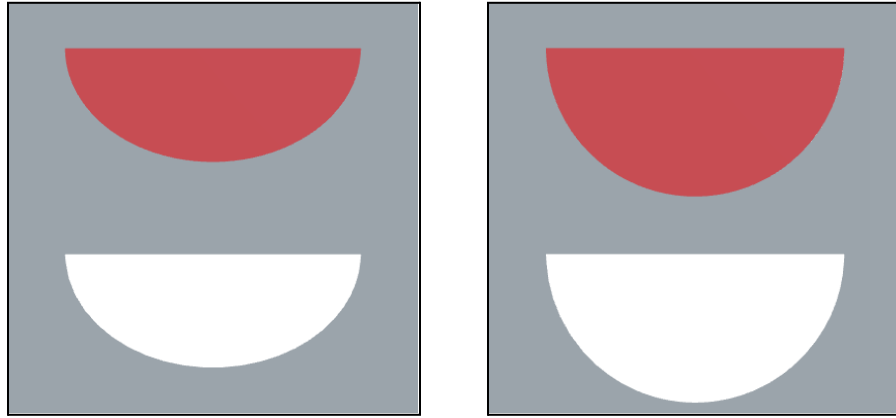


Figure 9: Channel size differences, Small (left) and Large (right).

For each of the channel sizes, simulations were performed for laminar and turbulent regimes, of which the results can be seen below in Figure 10. Under the laminar and turbulent regimes, especially after  $\sim 20\text{mm}$ , there is no significant difference in MTC between the different channel sizes in the magnitudes of the peaks and valleys. These peaks and valleys occur right after and before a bend in the channel, respectively, and this pattern occurs due to the zigzag nature of the channels in this and for every future study. For further inspection, Table 2 below tabulates the average MTC for each channel size under both regimes.

Channel Size	Average MTC [m/s]	
	Laminar Regime	Turbulent Regime
Small	3.9022E-04	1.1383E-03
Large	3.9971E-04	1.1770E-03

Table 2: Average MTC for each channel size under both regimes.

From Table 2, under both regimes, the Large channel size has slightly larger MTCs than the Small channel size. Although from Figure 10, most of the difference in the turbulent regime comes from the first 20mm of channel length, while in the laminar regime it can be argued that the Large channel has larger peaks than the small channel resulting in an overall greater MTC. Even if there is no significant difference in the MTC in either regime, using the Small channel comes with a cost.

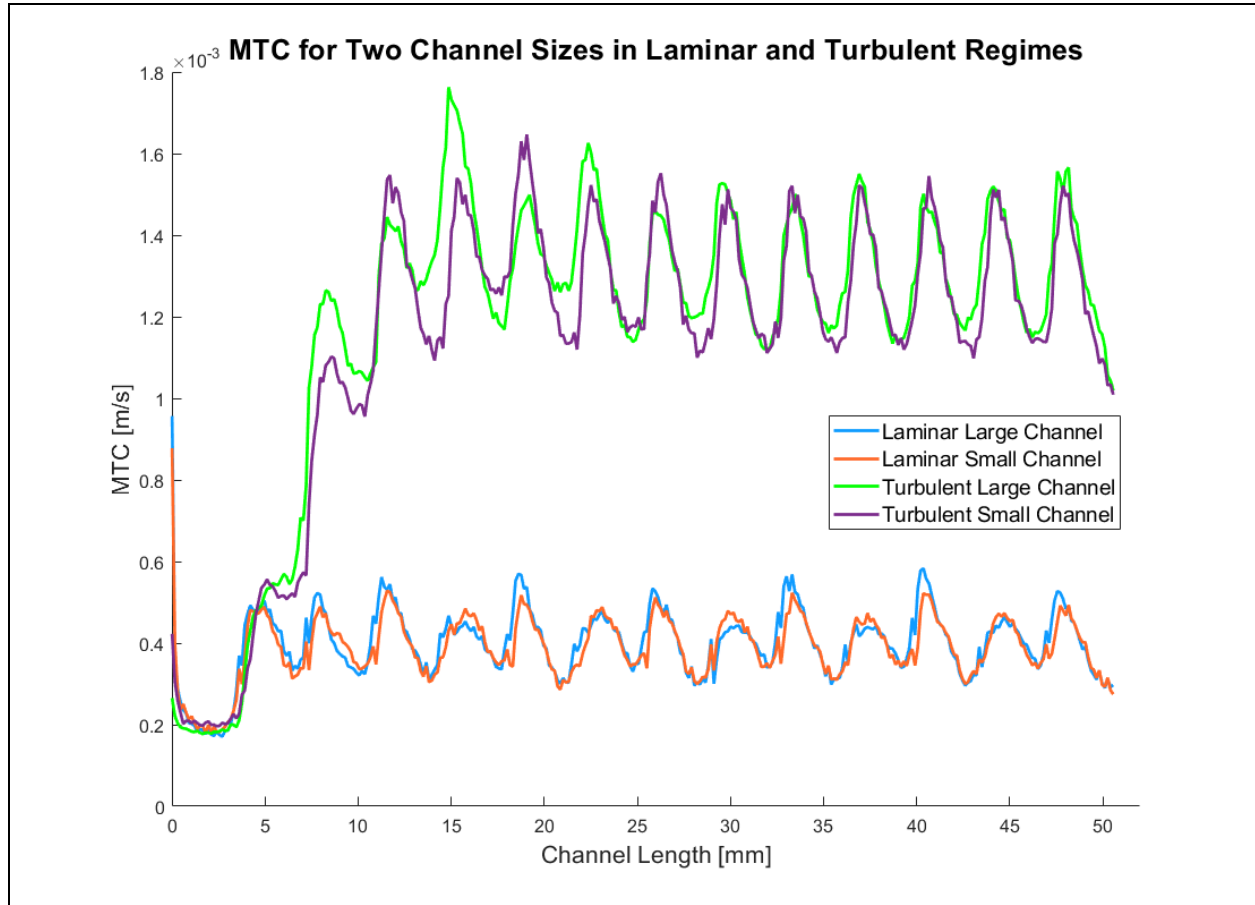


Figure 10: MTC over channel length for Small and Large channel sizes under laminar and turbulent regimes.

Another product of the channel size differences is shown in Table 3 below, which tabulates the flow rate-normalized pressure drop across the FLiBe channels. The rationale for normalization is to compare how much pumping power would be needed to transport the same amount of FLiBe in each geometry. From Table 3, a smaller channel size also has a significant impact on the pressure drop. Under the laminar regime, the Small channel size has a 16.83% larger drop, and under the turbulent regime has a 8.89% larger drop. All in all the Large channel is more preferable, as the pressure drops are lower and have a similar, if not slightly better, MTC.

Channel Size	Flow Rate-Normalized Pressure Drop [Pa/(m <sup>3</sup> /s)]	
	Laminar Regime	Turbulent Regime
Small	4.65E+07	4.90E+08
Large	3.98E+07	4.50E+08

Table 3: Flow rate-normalized pressure drops for each channel size under both regimes.

### Channel Orientation Study

For the channel orientation study, the team investigated four different orientations. Below in



Figure 11 shows the orientation differences. The first orientation has one FLiBe channel and one vacuum channel vertically stacked on top of one another and is called “1-1 Vertical.” The second orientation has the channels sit side-by-side, named “1-1 Horizontal.” The third orientation has stacked channels like the first but the FLiBe channel is flipped upside down, named “Burger.” Lastly, the final orientation instead stacks one more FLiBe channel below the vacuum channel, named “2-1.”

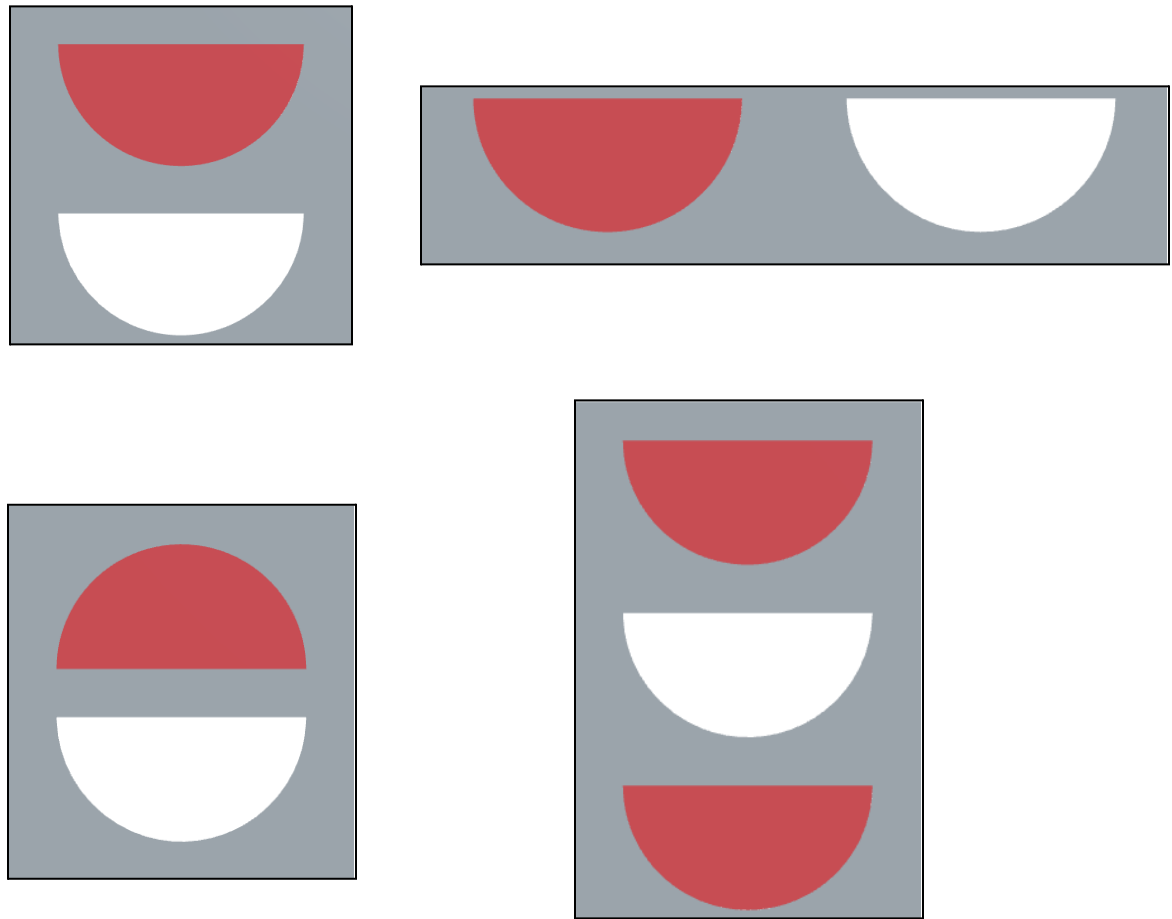


Figure 11: Channel orientation differences: 1-1 Vertical (top left), 1-1 Horizontal (top right), Burger (bottom left), and 2-1 (bottom right). Red indicates FLiBe channel and white indicates vacuum.

For each orientation, simulations were performed for laminar and turbulent regimes, of which the results can be seen below in Figure 12. Under both regimes (but more easily seen in the turbulent regime), the 1-1 Vertical and Burger orientations have greater MTCs than the 1-1 Horizontal and 2-1 orientations, with 2-1 performing the worst. Table 4 lists the average MTC for all of these orientations. The largest difference of MTCs, from the 2-1 to the 1-1 Vertical orientation, are 21.16% and 69.50% under the laminar and turbulent regimes respectively.

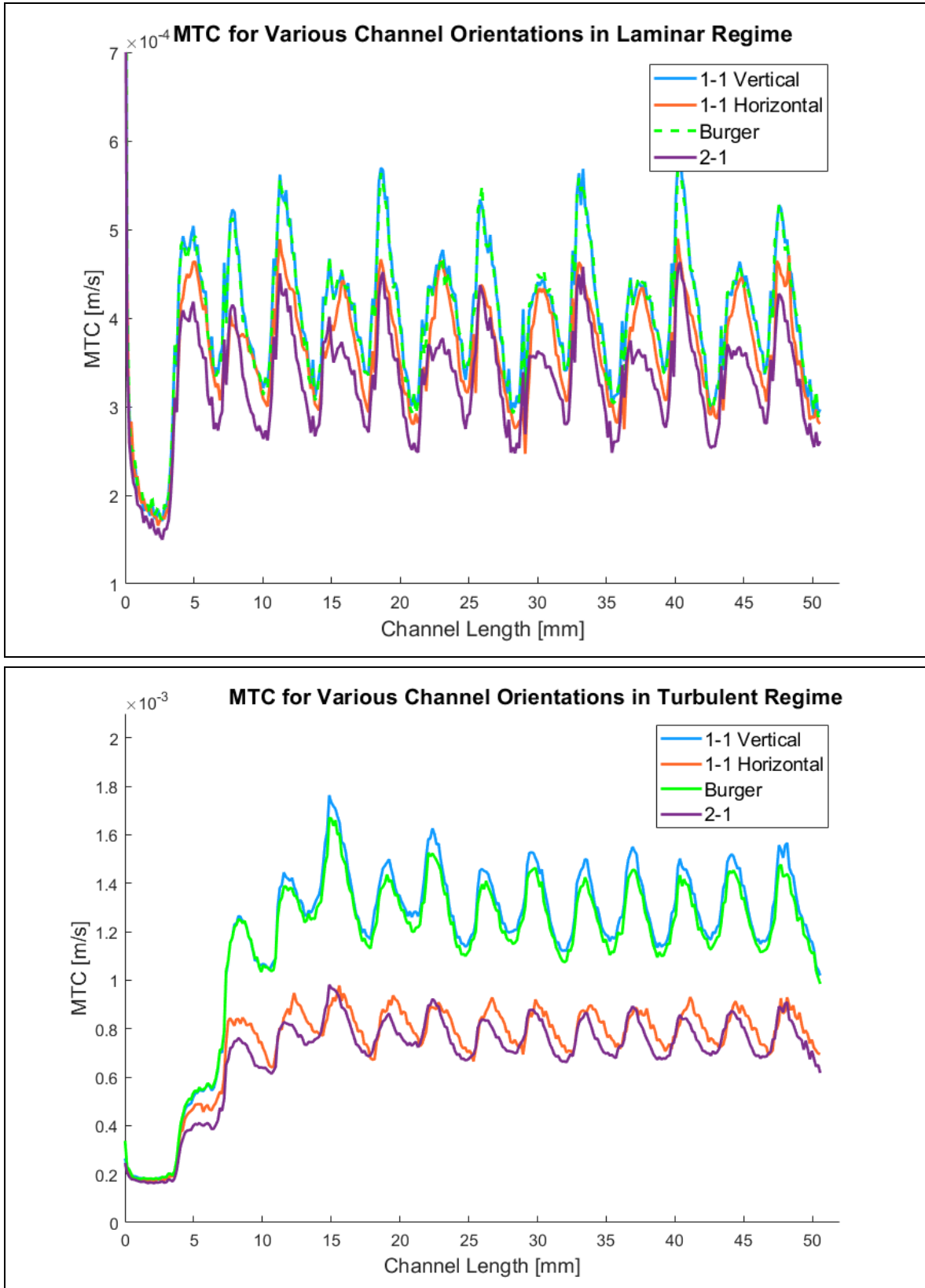


Figure 12: MTC over channel length for each orientation under laminar (top) and turbulent (bottom) regimes.

	Average MTC [m/s]	
Orientation	Laminar Regime	Turbulent Regime
1-1 Vertical	3.9971E-04	1.1770E-03
1-1 Horizontal	3.5998E-04	7.4196E-04
Burger	3.9846E-04	1.1395E-03
2-1	3.2990E-04	6.9438E-04

Table 4: Average MTC for each orientation under both regimes.

There are a few reasons why the 1-1 Horizontal and 2-1 orientations may have performed poorly. For the 2-1 orientation, since there are twice as many FLiBe channels as vacuum channels, there is more space in the 316SS for tritium to diffuse into without necessarily traveling towards a vacuum channel (i.e. between the FLiBe channels). While in the case of the 1-1 Horizontal orientation, the MTC may be lower due to the thickness of 316SS between the channels being greater than in the 1-1 Vertical or Burger orientations, leading to a less steep concentration gradient in the 316SS.

Table 5 below, which details the flow rate-normalized pressure drops across the FLiBe channels, shows the turbulent regime has much more significant pressure drops than laminar regimes. Thus, it would take much more power to drive the same amount of FLiBe under the turbulent regimes, making it a less viable option for a commercial application regardless of orientation.

	Flow Rate-Normalized Pressure Drop [Pa/(m <sup>3</sup> /s)]	
Orientation	Laminar Regime	Turbulent Regime
1-1 Vertical	3.98E+07	4.50E+08
1-1 Horizontal	3.97E+07	4.50E+08
Burger	3.97E+07	4.50E+08
2-1	3.96E+07	4.50E+08

Table 5: Flow rate-normalized pressure drops for each orientation under both regimes.

#### Zigzag bend angle study

From the control zigzag geometry (100 degrees), changing the bend angles should alter the mass transfer. Bend angles studied include 60, 100, 140, and 180 (straight) degrees as seen in Table 6. Channel diameter perpendicular to the flow is kept constant as well as the segment lengths at 4.75mm long. The total flow length is preserved across all four geometries. The team initially predicted that sharper angles would induce greater turbulence, reduce boundary layers, and increase heat and mass transfer. Additionally, acute angles were predicted to pose an issue for the

pressures required to drive the fluid flow.





180 degrees	140 degrees
	
100 degrees	60 degrees
	

Table 6: The 4 bend angle geometries being studied

The results of the bend angle study are shown in Figure 13 as plots of MTC as a function of distance along the channel. It can be clearly seen that the 60 and 100 degree angle geometries with turbulent models (60 Turb and 100 Turb) outperform the other angles with respect to their overall MTC values. Consistent with the previous channel size and orientation studies, each bend angle geometry showed increased MTC with turbulent flow compared to laminar flow. The periodic nature of many of these plots is due to the angles of the channel. The peaks and valleys of the plots correspond directly with the bends in the channel as shown in Figure 14. Low MTC amplitudes are exhibited in 140 Turb, 180 Turb, and 180 Laminar.

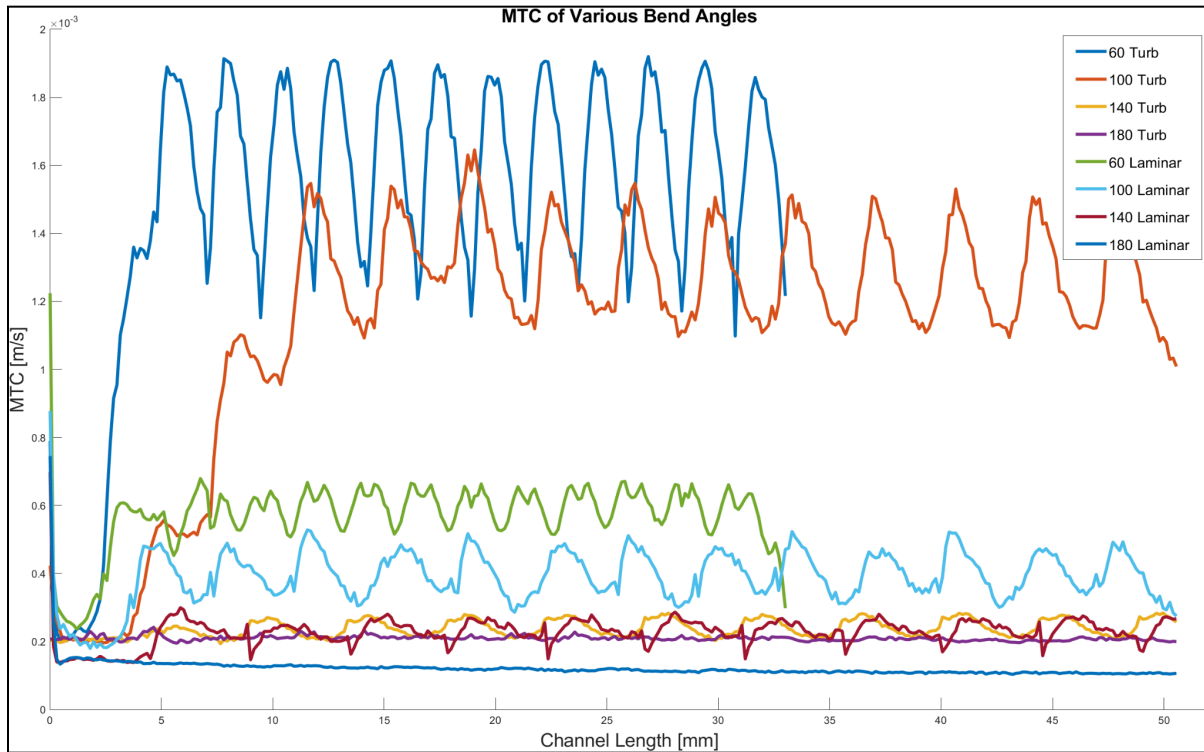


Figure 13: Mass transfer coefficient (MTC) as a function of distance along the channels for varying channel bend angles and flow rates.

The angle geometries that don't exhibit prominent peaks and valleys (amplitudes) can be attributed to the fluid flow not crashing into the walls of the channel as much and maximum velocities not reaching as high. The flow velocities in Figure 14 show the increasing velocities and 'wall crashing' as the bend angle decreases. The 140 Turb and 140 Laminar have similar MTC profile plots and the team believes that this similarity is due to the flow in their channels behaving quite similar to each other in both the turbulent and laminar flow regimes.

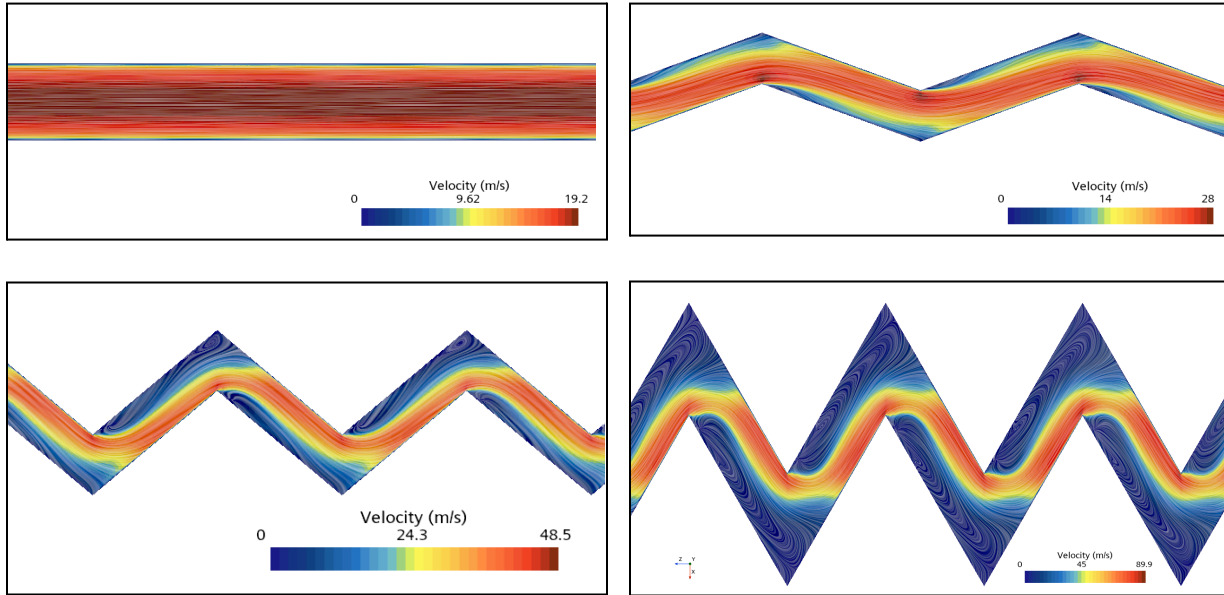


Figure 14: Top-down cut-section view of the turbulent velocity profiles in 180 (top-left), 140 (top-right), 100 (bottom-left) and 60 (bottom-right) channels

Table 7 summarizes the average MTC values for each channel geometry. What is more clear with these averaged values is the decreasing MTC as the channel bend angle increases. This trend makes sense as higher angles up to 180 degrees get more and more straight, leading to less turbulent mixing of the FLiBe and less mass transfer. Conversely, as the bend angle decreases and the flow has to make sharper turns, there is more turbulent mixing and more mass transfer.

Channel Bend Angle	Average MTC [m/s]	
	Laminar Regime	Turbulent Regime
60	4.496E-04	1.430E-03
100	2.997E-04	1.108E-03
140	1.601E-04	2.259E-04
180	7.652E-05	1.986E-04

Table 7: Average MTC for each orientation under both regimes.

It is important to note that the high MTC values achieved by lower bend angles come at a cost.

Table 8 summarizes the flow-rate-normalized pressure drop through the channels for each geometry. While it is clear that higher MTC values can be achieved by increasing turbulent mixing and decreasing the bend angle, the pressure required to drive such a flow increases drastically. Moving from 100 to 60 degrees in laminar, there's a 50% increase in MTC at a cost of 5.4 times the pressure. And in the turbulent case, there's a 29.1% increase in MTC at a cost of 6.6 times the pressure. Hence, it must be noted that with increased MTC from decreased bend angle, there is a tradeoff in pressure and energy required to drive flow.

	<b>Flow Rate-Normalized Pressure Drop [Pa/(m<sup>3</sup>/s)]</b>	
<b>Channel Bend Angle</b>	<b>Laminar Regime</b>	<b>Turbulent Regime</b>
<b>60</b>	2.50E+08	3.22E+09
<b>100</b>	4.65E+07	4.90E+08
<b>140</b>	1.76E+07	8.55E+07
<b>180</b>	1.33E+07	3.37E+07

Table 8: Flow rate-normalized pressure drops for each orientation under both regimes.

Taking a closer look at the effect of flow on the MTC values, the average MTC against the Reynolds number is plotted in Figure 15. As desired, there is a clear separation between the Reynolds numbers for laminar versus turbulent flow. What is surprising is that some of the laminar flow geometries outperform some of the turbulent flow geometries. Specifically the 100 and 60 degree geometries in laminar exhibit higher average MTC values than the 180 and 140 geometries in turbulent flow. These relationships hint that desirable MTC values can be achieved with lower flow rates and lower energy expenditure.

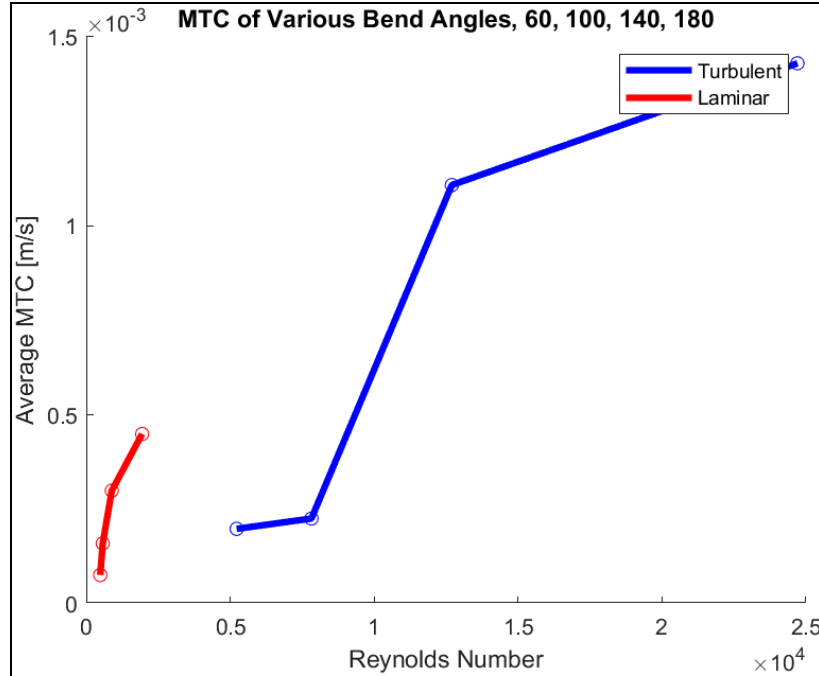


Figure 15: Plot of average MTC with respect to Reynolds number. Four points are plotted for laminar and turbulent flow regimes with the plots showing increasing Reynolds numbers for decreasing bend angle.

Taking a closer look at the effect of pressure, the average MTC against the flow-rate normalized pressure drop is plotted in Figure 16. There are orders of magnitude differences between the pressures, so it is plotted using log-scale. The previous figure established that some of the geometries in the laminar regime outperformed other geometries in the turbulent regime. Looking at the figure below, it is interesting to see the geometries that outperformed also had overlapping pressure drops, visually reemphasizing the energy required to drive the fluid in order to achieve a desired MTC.

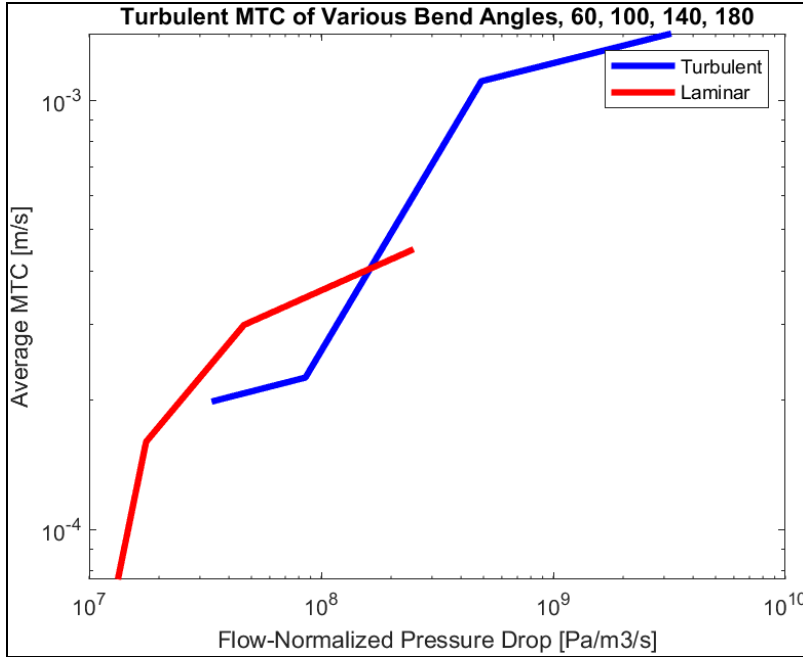


Figure 16: Plot of average MTC with respect to flow-normalized pressure drop. Four points are plotted for laminar and turbulent flow regimes with the plots showing increasing pressure drop for decreasing bend angle.

#### Segment length study

Similar to the channel bend angle study, the segment length study aims to determine the effect of varying the length of each segment. The control segment length is 4.75mm and the study runs through lengths of 2.375, 3.56, and 9.5 mm.

Figure 17 presents a top view of the velocity field. Although the inlet velocity is set to 15 m/s, the team observed that the flow accelerates as it stretches and the cross-sectional area narrows. This top-view visualization is complemented by a graph showing the mass transfer coefficient (MTC) along the z-axis. The MTC values are from past simulations, however the behaviour is the same as the current simulations. Local maxima occur where the flow impinges on the next wall of the zig-zag structure, while MTC decreases as the flow develops along the wall.

This behavior motivates the segment length study: the team hypothesized that longer segments would result in lower relative minima due to extended flow development, while shorter segments would maintain higher MTC levels by limiting this development. It was predicted that as segment length decreases, there would be more frequent fluid boundary layer break-up, leading to enhanced heat and mass transfer. Therefore, shorter lengths were expected to yield better mass transfer performance.



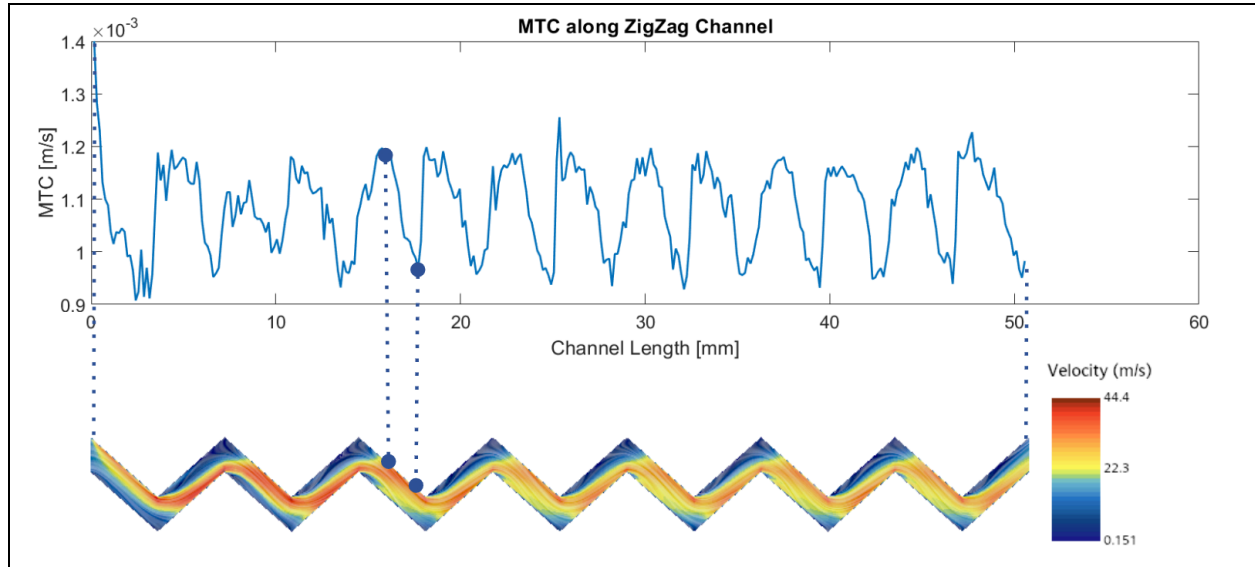


Figure 17: Top View of Velocity Field and Its Influence on Mass Transfer Coefficient Along the Z-Axis

To validate this hypothesis, different segment lengths were tested: the original, double, half, and three-quarters of the original. Then each case was simulated to compare their effects on the MTC. As shown in Figure 18, the turbulent flow consistently demonstrates a higher MTC than the laminar case. Overall, the peak MTC values remain within the same order of magnitude between laminar and turbulent flows, except for the turbulent double-length case. When the segment length is increased, the MTC exhibits a more prolonged decline between successive peaks, resulting in a lower overall mean MTC value. This confirms the team's hypothesis that extended flow development in longer segments reduces the average mass transfer performance.

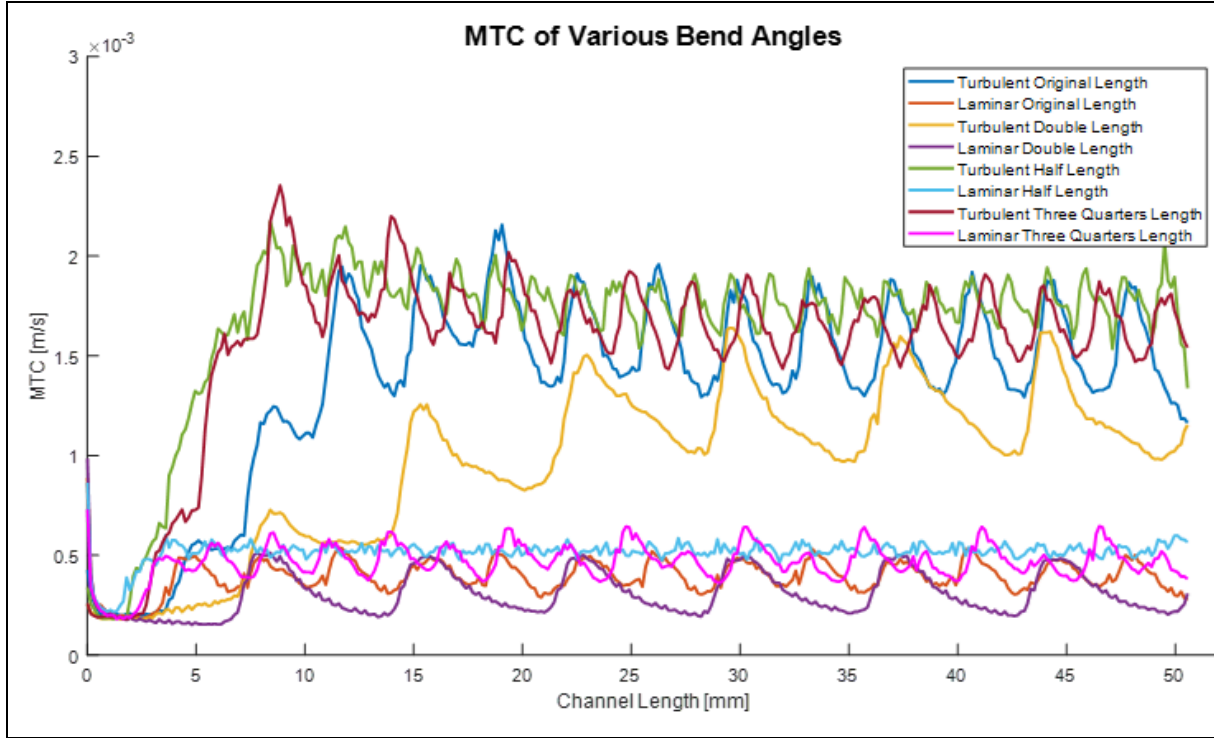


Figure 18: Mass transfer coefficient (MTC) as a function of distance along the channels for varying channel length segments and flow rates.

Table 9 summarizes the average MTC values for each channel geometry. These values confirm the trend observed in Figure 18: the turbulent regime exhibits higher MTC than the laminar regime. Additionally, the results show that shorter segment lengths lead to improved MTC performance, further supporting the team's hypothesis. One important thing to note is that reducing the segment lengths indefinitely will not indefinitely increase the MTC. This is because at the smallest segment length possible, the geometry becomes a straight channel and has suboptimal MTC performance. Therefore, there must be an optimal segment length for MTC between the half length segments and “no length” segments.

Channel Segment Length (mm)	Average MTC [m/s]	
	Laminar Regime	Turbulent Regime
2.375	5.1608E-04	1.7E-3
3.56	4.6672E-04	1.6E-3
4.75	3.9572E-04	1.4E-03
9.5	3.0885e-04	9.5406E-04

Table 9: Average MTC for each orientation under both regimes.

Similarly to the angle bend study, an important note is that the high MTC values achieved by lower bend angles come at a cost. Table 10 summarizes the flow-rate-normalized pressure drop

through the channels for each geometry. While it is clear that higher MTC values can be achieved by increasing turbulent mixing and decreasing the segment length, the pressure required to drive such a flow increases drastically. Moving from 4.75 to 2.375 mm in laminar regime, there's a 30% increase in MTC at a cost of 76% increase of the pressure. And in the turbulent regime case, there's a 21% increase in MTC at a cost of 2.55 times the pressure. Hence, it must be noted that with increased MTC from decreased segment length, there is a tradeoff in pressure and energy required to drive flow.

	<b>Flow Rate-Normalized Pressure Drop [Pa/(m<sup>3</sup>/s)]</b>	
<b>Channel Segment Length (mm)</b>	<b>Laminar Regime</b>	<b>Turbulent Regime</b>
<b>2.375</b>	8.19E+07	1.25E+09
<b>3.56</b>	6.59E+07	7.86E+08
<b>4.75</b>	4.65E+07	4.90E+08
<b>9.5</b>	3E+07	2.25E+08

Table 10: Flow rate-normalized pressure drops for each orientation under both regimes.

#### Main Takeaways and Recommendations for Future Designs to Optimize Tritium Extraction

The team has examined the use of a printed circuit heat exchanger (PCHE) for tritium extraction from molten salt (FLiBe). PCHEs were studied for how its design parameters influenced mass transfer. The parameters include channel size, orientation, bend angle, and segment length. For each parameter, the team looked at the MTC along the channels, the average MTC, and the flow-rate normalized pressure drop across the channel. The MTC showed how quickly mass (tritium) was being removed from the FLiBe and the pressure drop indicated relatively how much energy would be required to drive the flow in each geometric case.

Overall conclusions can be summarized as follows: in the channel size study, a larger channel size has a slight positive impact on the MTC under both regimes. Additionally, a larger channel decreases the pressure drop for both regimes. Thus, a smaller channel may not be preferable due to the increased need for power to pump the FLiBe, especially if the turbulent regime is utilized. Future investigation into even larger channel sizes may be worthwhile to find if and when the pressure drop plateaus and if the MTC could be driven higher. In the channel orientation study, the 1-1 Vertical and Burger orientations performed the best, indicating that having more FLiBe channels than vacuum and having a farther distance between the channels may drive the MTC down.

In the channel angle study, a higher MTC results from smaller bend angles, but at the cost of drastically increasing the pressure drop across the channel. A middle ground between mass transfer and pressure drop must be selected based on application. In the segment length study, it is determined that a shorter segment length leads to a higher MTC, pointing to the fact that high MTC is the result of 'stagnation points' in which the fluid FLiBe crashes into the channel walls and breaks the velocity boundary layer. This simultaneously is what happens in a heat exchanger,

where the stagnation points have the highest heat transfer rate. This once again leads to the conclusion that the PCHE that has been designed for high heat transfer will work well for the mass transfer of tritium.

In summary, increases in MTC are consistently associated with higher pressure drops. The optimal channel geometry will ultimately depend on the specific application and the acceptable balance between mass transfer efficiency and pumping power requirements. The team can confidently say that the PCHE, which has been designed for increased heat transfer, is also good for increased mass transfer of tritium from FLiBe.

For future work, there are three important studies that can be performed. First, using the K-Omega Turbulent model instead of the K-Epsilon Turbulent Model used. This model selection may help with the accuracy of the simulation as with the K-Omega model, one does not have to worry about having a liquid boundary prism layer thickness on the order of  $y^+$ . Second, running a PCHE material study would be interesting if possible. The study could include using different metals for the PCHE such as carbon steel, Vanadium, Hastelloy, and more. The caveat to this study would be that diffusion constants and other physical interactions would need to be known for the metal and these might not exist in literature yet. Lastly, any and all studies bring us to the third path forward – physical testing and validation. Running physical experiments to validate the simulations that have been performed in the project is key to ensuring companies can trust the data and can move forward with accurate knowledge in their commercial operations.

## References

- [1]  
G. Ferrero, S. Meschini, and R. Testoni, “A Preliminary CFD and Tritium Transport Analysis for ARC Blanket,” *Fusion Science and Technology*, vol. 78, no. 8, pp. 617–630, Nov. 2022, doi: [10.1080/15361055.2022.2096365](https://doi.org/10.1080/15361055.2022.2096365).
- [2]  
Y. Zeng, Q. Zhang, K. Deng, and W. Liu, “A simulation study of tritium distribution in a 10WM(e) thorium-based molten salt reactor,” *Annals of Nuclear Energy*, vol. 197, p. 110272, Mar. 2024, doi: [10.1016/j.anucene.2023.110272](https://doi.org/10.1016/j.anucene.2023.110272).
- [3]  
B. N. Sorbom *et al.*, “ARC: A compact, high-field, fusion nuclear science facility and demonstration power plant with demountable magnets,” *Fusion Engineering and Design*, vol. 100, pp. 378–405, Nov. 2015, doi: [10.1016/j.fusengdes.2015.07.008](https://doi.org/10.1016/j.fusengdes.2015.07.008).
- [4]  
B. Garcinuño *et al.*, “Design and fabrication of a Permeator Against Vacuum prototype for small scale testing at Lead-Lithium facility,” *Fusion Engineering and Design*, vol. 124, pp. 871–875, Nov. 2017, doi: [10.1016/j.fusengdes.2017.02.060](https://doi.org/10.1016/j.fusengdes.2017.02.060).
- [5]  
M. Utili *et al.*, “Design and Integration of the WCLL Tritium Extraction and Removal System into the European DEMO Tokamak Reactor,” *Energies*, vol. 16, no. 13, Art. no. 13, Jan. 2023, doi: [10.3390/en16135231](https://doi.org/10.3390/en16135231).
- [6]  
G. G. Fonfría, F. R. Ugorri, and D. Rapisarda, “Direct numerical simulations of tritium extraction in PbLi-based breeding blankets in the laminar–turbulent transition region,” *International Journal of Heat and Mass Transfer*, vol. 231, p. 125771, Oct. 2024, doi: [10.1016/j.ijheatmasstransfer.2024.125771](https://doi.org/10.1016/j.ijheatmasstransfer.2024.125771).
- [7]  
J. A. Teprovich, H. R. Colon Mercado, L. Olson, P. Ganesan, D. Babineau, and B. L. Garcia-Diaz, “Electrochemical extraction of hydrogen isotopes from Li/LiT mixtures,” *Fusion Engineering and Design*, vol. 139, pp. 1–6, Feb. 2019, doi: [10.1016/j.fusengdes.2018.11.018](https://doi.org/10.1016/j.fusengdes.2018.11.018).
- [8]  
K. Dolan, G. Su, and G. Zheng, “Experimental Measurement and Multiphysics Simulation of Tritium Transport in Neutron-Irradiated Flibe Salt,” *Nuclear Technology*, Jan. 2023. Accessed: Jan. 14, 2025. [Online]. Available:

[https://drive.google.com/file/u/1/d/1pMYLMzkl8OLTSeatvNebXH4u-oyVVPFR/view?usp=embed\\_facebook](https://drive.google.com/file/u/1/d/1pMYLMzkl8OLTSeatvNebXH4u-oyVVPFR/view?usp=embed_facebook)

[9]

A. Trautmann, G. Mori, M. Oberndorfer, S. Bauer, C. Holzer, and C. Dittmann, “Hydrogen Uptake and Embrittlement of Carbon Steels in Various Environments,” *Materials (Basel)*, vol. 13, no. 16, p. 3604, Aug. 2020, doi: [10.3390/ma13163604](https://doi.org/10.3390/ma13163604).

[10]

P. Calderoni, P. Sharpe, M. Hara, and Y. Oya, “Measurement of tritium permeation in flibe (2LiF–BeF<sub>2</sub>),” *Fusion Engineering and Design*, vol. 83, no. 7, pp. 1331–1334, Dec. 2008, doi: [10.1016/j.fusengdes.2008.05.016](https://doi.org/10.1016/j.fusengdes.2008.05.016).

[11]

Y. Li, Z. Qiu, D. Cui, Z. Wang, J. Zhang, and Y. Ji, “Numerical investigation on the thermal-hydraulic performance of helical twine printed circuit heat exchanger,” *International Communications in Heat and Mass Transfer*, vol. 128, p. 105596, Nov. 2021, doi: [10.1016/j.icheatmasstransfer.2021.105596](https://doi.org/10.1016/j.icheatmasstransfer.2021.105596).

[12]

“Study: Fusion energy could play a major role in the global response to climate change,” MIT News | Massachusetts Institute of Technology. Accessed: Apr. 29, 2025. [Online]. Available: <https://news.mit.edu/2024/fusion-energy-could-play-major-role-global-response-climate-change-1024>

[13]

M. Saeed and M.-H. Kim, “Thermal and hydraulic performance of SCO<sub>2</sub> PCHE with different fin configurations,” *Applied Thermal Engineering*, vol. 127, pp. 975–985, Dec. 2017, doi: [10.1016/j.applthermaleng.2017.08.113](https://doi.org/10.1016/j.applthermaleng.2017.08.113).

[14]

“What is y+ (yplus)? - Using SimScale / Fluid Flow / CFD,” SimScale CAE Forum. Accessed: Apr. 29, 2025. [Online]. Available: <https://www.simscale.com/forum/t/what-is-y-yplus/82394>

## Appendix

### Appendix A.1: Physical Constants and Properties of FLiBe and 316SS

Physical Constants and Properties in STAR-CCM+	Definition
$\frac{\partial}{\partial t} \oint_V \rho \phi dV + \oint_A \rho \phi \bar{v} \cdot d\bar{a} = \oint_A \bar{j} \cdot d\bar{a} + \oint_V S_\phi dV$	Transport equation for passive scalar in a fluid t = time ρ = density V = volume $\bar{v}$ = velocity A = area $\bar{j}$ = diffusion flux $S_\phi$ = passive scalar source term
T	Temperature of FLiBe or 316SS, as contextually necessary
$0.427 * e^{\frac{-13.9}{0.008314*T}}$	K316: Sievert's law coefficient for passive scalar in 316SS
$1.6 * 10^{-5} * e^{\frac{-28}{0.008314*T}}$	KFLiBe: Henry's law coefficient for passive scalar T2 in FLiBe
$\frac{1}{\sqrt{3}} 6.32 e^{\frac{-47.8}{0.008314*T}} * 10^{-7}$	D316: Molecular diffusivity of passive scalar (tritium) in 316SS
$9.3 e^{\frac{-47.8}{0.008314*T}} * 10^{-7}$	DFLiBe: Molecular diffusivity of passive scalar (tritium) in FLiBe
$8084.2 - 0.42086T - 3.8942T^2 * 10^{-5}$	316 Density: Density of 316 Stainless Steel
$2413 - 0.488T$	Salt Density: Density of FLiBe as a function of temperature in fluid form
$\frac{(T_{316BoundaryFlux})}{(316\ Density)}$	316 Boundary Flux: Flux of passive scalar through the salt-316 boundary  T_316BoundaryFlux is from and is populated by StarCCM+
$(KFLiBe) \sqrt{P_{T2} K_{eq} \left( \frac{T_{2\ 316}}{K_{316}} \right)^2}$	T_Eq_Wall_K: Passive scalar concentration in FLiBe at the steel interface, coupled with tables to transport the passive scalar to the stainless steel

$\frac{(T2 \text{ SaltBoundaryFlux})(316 \text{ Density})}{(\text{Salt Density})}$	<p>Salt-&gt;316 Boundary Flux: The equivalent flux of a solid material if it were to behave like a fluid with the given fluid density, based on the original flux of the solid material. Comparing flow rate of passive scalar from fluid to solid while taking into account the different densities involved</p> <p>T2 SaltBoundaryFlux is from and is populated by StarCCM+</p>
$\frac{(T2 \text{ SaltBoundaryFlux})}{(\text{Salt Density})}$	<p>Salt Boundary Flux: Flux of the passive scalar at the FLiBe boundary</p> <p>T2 SaltBoundaryFlux is from and is populated by StarCCM+</p>
$0.000116e^{\frac{3755}{T}}$	FLiBe dynamic viscosity as a function of temperature
T_Eq_Wall_K	Internal table used to store the passive scalar in FLiBe at the salt-316 boundary
Salt->316 Boundary Flux	Internal table used to track the flux of passive scalar from the salt to 316SS

Table 11: Table of STAR-CCM+ Field Functions and Tables



Appendix A.2: Simulation Continua Physical Models Chosen

Continua for Each Material Modeled				
Simulation (velocity and passive scalar separated to simplify calculations)	Laminar		Turbulent	
	FLiBe	316 Stainless Steel	FLiBe	316 Stainless Steel
Velocity Simulation	Coupled Energy	Coupled Energy	Coupled Energy	Coupled Energy
	Coupled Flow	Coupled Flow	Coupled Flow	Coupled Flow
	Gradients	Gradients	Gradients	Gradients
	Laminar	Laminar	K-Epsilon Turbulence	Laminar
	Liquid (FLiBe Custom)	Liquid (316 Stainless Steel Custom)	Liquid (FLiBe Custom)	Liquid (316 Stainless Steel Custom)
	Polynomial Density	Polynomial Density	Polynomial Density	Polynomial Density
	Solution Interpolation	Solution Interpolation	Realizable K-Epsilon Two-Layer	Solution Interpolation
	Steady	Steady	Reynolds-Avera ged Navier-Stokes	Steady
	Three Dimensional	Three Dimensional	Solution Interpolation	Three Dimensional
	Wall Distance		Steady	
			Three Dimensional	
			Turbulent	
			Two-Layer All y+ Wall Treatment	
			Wall Distance	

Passive Scalar Simulation	Coupled Energy	Coupled Energy	Coupled Energy	Coupled Energy
	Coupled Flow	Coupled Flow	Coupled Flow	Coupled Flow
	Gradients	Gradients	Gradients	Gradients
	Laminar	Laminar	K-Epsilon Turbulence	Laminar
	Liquid (FLiBe Custom)	Liquid (316 Stainless Steel Custom)	Liquid (FLiBe Custom)	Liquid (316 Stainless Steel Custom)
	<u>Passive Scalar</u>	<u>Passive Scalar</u>	<u>Passive Scalar</u>	<u>Passive Scalar</u>
	Polynomial Density	Polynomial Density	Polynomial Density	Polynomial Density
	Solution Interpolation	Solution Interpolation	Realizable K-Epsilon Two-Layer	Solution Interpolation
	Steady	Steady	Reynolds-Averaged Navier-Stokes	Steady
	Three Dimensional	Three Dimensional	Solution Interpolation	Three Dimensional
	Wall Distance		Steady	
			Three Dimensional	
			Turbulent	
			Two-Layer All y+ Wall Treatment	
			Wall Distance	

Table 12: Continua Physics Model settings for FLiBe and 316SS regions under laminar and turbulent regimes.

### Appendix A.3: Inlet Tritium Concentration Calculation

First, there are a few given values from ARC conditions and other constants used for the calculation of the inlet BC tritium concentration [1]:

$$FLiBe \text{ Flow Rate } \left[ \frac{m^3}{s} \right] = 1.08$$

$$Tritium \text{ Burnup } \left[ \frac{kg}{s} \right] = 9 \times 10^{-7}$$

$$Tritium \text{ Breeding Ratio (TBR)} = 1.1$$

$$g/mol \text{ of } T2 = 6.032$$

From these values, tritium production in FLiBe in kg/s is calculated and then translated into mol/s:

$$\begin{aligned} Tritium \text{ Production in FLiBe } \left[ \frac{mol}{s} \right] &= TBR \times Tritium \text{ Burnup} \div (6.032 \text{ g/mol}) \\ &= 1.64 \times 10^{-4} \text{ mol/s} \end{aligned}$$

Lastly, FLiBe flow rate is calculated to solve for the average tritium concentration in FLiBe:

$$\begin{aligned} Tritium \text{ Concentration in FLiBe } \left[ \frac{mol}{m^3} \right] &= Tritium \text{ Production in FLiBe} \div FLiBe \text{ Flow Rate} \\ &= 1.52 \times 10^{-4} \text{ mol/m}^3 \end{aligned}$$

#### Appendix A.4: Simulation Mesh Settings Chosen

Mesh Setting	Mesh Settings Choice for Each Material Modeled			
	Laminar		Turbulent	
	FLiBe	316 Stainless Steel	FLiBe	316 Stainless Steel
Meshers	Polyhedral Mesher Surface Remesher Prism Layer Mesher Automatic Surface Repair	Polyhedral Mesher Surface Remesher Prism Layer Mesher Automatic Surface Repair	Polyhedral Mesher Surface Remesher Prism Layer Mesher Automatic Surface Repair	Polyhedral Mesher Surface Remesher Prism Layer Mesher Automatic Surface Repair
Base Size	0.1mm	0.5mm	0.25mm	0.5mm
CAD Projection	On	On	On	On
Target Surface Size	80% Relative to Base	80% Relative to Base	80% Relative to Base	80% Relative to Base
Minimum Surface Size	10% Relative to Base	10% Relative to Base	10% Relative to Base	10% Relative to Base
Surface Curvature	Curvature Deviation Distance Off	Curvature Deviation Distance Off	Curvature Deviation Distance Off	Curvature Deviation Distance Off
Surface Proximity	0.0m Search Floor 2 Points in gap Search Ceiling Off	0.0m Search Floor 2 Points in gap Search Ceiling Off	0.0m Search Floor 2 Points in gap Search Ceiling Off	0.0m Search Floor 2 Points in gap Search Ceiling Off
Surface Growth	1.2	1.2	1.2	1.2

Rate				
Auto-Repair Minimum Proximity	0.01	0.01	0.01	0.01
Volume Growth Rate	1.2	1.2	1.2	1.2
Maximum Tet Size	10000% Relative to base (set very large)	10000% Relative to base (set very large)	10000% Relative to base (set very large)	10000% Relative to base (set very large)
Core Mesh Optimization	1 Cycle 0.4 Threshold	1 Cycle 0.4 Threshold	5 Cycles 1 Threshold	1 Cycle 0.4 Threshold
Post Mesh Optimization	All off	All off	All on	All off
Prism Layer Setting	Prism Layer Settings Choice for Each Material Modeled			
	Laminar		Turbulent	
	FLiBe	316 Stainless Steel	FLiBe	316 Stainless Steel
Number of Prism Layers	5	0	3	0
Prism Layer Stretching	1.2	N/A	1.2	N/A
Prism Layer Reduction Percentage	50%	N/A	0	N/A
Concave Angle Limit	0 deg	N/A	0 deg	N/A

Convex Angle Limit	360 deg	N/A	360 deg	N/A
Near Core Layer Aspect Ratio	0	N/A	0.5	N/A
Gap Fill Percentage	25%	N/A	25%	N/A
Minimum Thickness Percentage	10%	N/A	5%	N/A
Boundary March Angle	50 deg	N/A	50 deg	N/A
Prism Layer Total Thickness	50% Relative to base	N/A	0.15mm Absolute	N/A

Table 13: Bulk Mesh and Prism Layer settings for FLiBe and 316SS regions under laminar and turbulent regimes.